B-Spline Surface-Based Reduced-Order Modeling of Nonplanar Crack Growth in Structural Digital Twins

Fubin Zhao*, Xuan Zhou†, Shuangxin He‡, Chaoyang Wang§, and Leiting Dong¶
Beihang University, 100191 Beijing, People's Republic of China

Satya N. Atluri‖
Texas Tech University, Lubbock, Texas, USA, 79409

Nonplanar crack growth holds a critical role in aeronautical structures, necessitating effective analysis under mixed fatigue loading to assess structural integrity. This study introduces a reduced-order modeling (ROM) method for predicting nonplanar crack growth in structural digital twins. The method's advantage lies in its representation of the entire crack surface morphology using a B-spline surface, which better captures its impact on crack growth. The symmetric Galerkin boundary element method - finite element method coupling method is adopted as a full-order method to generate the crack database. Isoparametric coordinates of the crack surface and stress intensity factor serve as input and output, respectively, for training the ROM, which integrates K-mean clustering, principal component analysis, and Gaussian process regression. The proposed approach is demonstrated using a rotorcraft mast-like component. Results reveal superior fracture mechanics parameter prediction compared to the crack-front-based ROM. Furthermore, the method boasts three orders of magnitude greater efficiency than full-order simulation, enabling its coupling with approaches like Monte Carlo for probabilistic crack growth analysis. Future work entails integrating our method into the probabilistic framework of digital twins.

Nomenclature

K_I	=	mode I stress intensity factor
K_{II}	=	mode II stress intensity factor
K_{eff}	=	equivalent stress intensity factor
α	=	crack growth angle

*Ph.D. candidate, School of Aeronautic Science and Engineering.
†Ph.D. candidate, School of Aeronautic Science and Engineering; zhoux@buaa.edu.cn (Co-Corresponding author).
‡Ph.D., School of Aeronautic Science and Engineering.
§Ph.D. candidate, School of Aeronautic Science and Engineering.
¶Professor & Deputy Dean, School of Aeronautic Science and Engineering; ltdong@buaa.edu.cn (Corresponding author).
‖Professor and Presidential Chair, Department of Mechanical Engineering; Fellow AIAA.

$C,\ m$	=	parameters in the modified Paris law
$u,\ v$	=	coordinate directions on the B-spline surface parameter space
$U,\ V$	=	node vectors in the directions of u and v
$N_{i,p}$	=	the i_{th} order basis function with polynomial order p
P	=	control point
D	=	given data point
a	=	crack length
$B,\ T$	=	applied bending moment and torque
$B_{base},\ T_{base}$	=	benchmark loads of bending moments and torques
$K_{I,B_{base}},\ K_{II,B_{base}}$	=	stress intensity factors under B_{base}
$K_{I,T_{base}},\ K_{II,T_{base}}$	=	stress intensity factors under T_{base}
$\boldsymbol{t}_{cf}$	=	unit vector tangent to the front edge of the crack surface
$\boldsymbol{n}_{cf}$	=	unit vector normal to the crack front and tangent to the crack surface
$\boldsymbol{n}_{cs}$	=	unit binormal vector normal to the crack surface
$\boldsymbol{e}_1,\ \boldsymbol{e}_2,\ \boldsymbol{e}_3$	=	global coordinate system
$\boldsymbol{C}$	=	spatial coordinates of a crack surface
$\varepsilon_{K_I},\ \varepsilon_{K_{II}}$	=	prediction error of K_I and K_{II}
e^d	=	prediction error of crack growth
θ	=	crack surface angle
e^θ	=	prediction error of crack surface angle

I. Introduction

Fatigue fracture is a common failure mode in aeronautical structures. Variances in fatigue crack shapes and sizes can arise due to mission histories within similar component types across diverse aircraft in a fleet [1]. Accurate fatigue crack growth prediction is essential for determining the remaining useful life and supporting inspection and maintenance decisions [2]. The U.S. Air Force has been funding research on airframe digital twins (ADT) since 2010 [3]. ADT provides proactive fleet maintenance support by creating multiphysics, multiscale, and probabilistic virtual models of built systems. The National Research Council of Canada also proposed probabilistic lifetime usage monitoring for helicopters [4], which can be considered a precursor to the concept of helicopter digital twins. The probabilistic nature of digital twins highlights the need for efficient crack growth analysis, which can be integrated into the digital twin's probabilistic framework to support real-time diagnosis and prognosis [5–10].

In contrast to aircraft structures, helicopter structures, such as rotor shafts and hubs, typically experience mixed

fatigue loads [11], resulting in a mixed-mode stress field near the crack front of damaged components [12]. This phenomenon leads to non-planar, three-dimensional crack growth, culminating in structural failure. Several methods, including three-dimensional finite element analysis, extended finite element analysis with enriched basis functions [13–16], and meshless methods [17, 18], have been developed to simulate this behavior. Despite their capacity to simulate non-planar crack growth, these methods still entail considerable time expenditure in the context of probabilistic crack growth analysis involving numerous queries.

ROM [19–23] can be leveraged to overcome the previously outlined limitations, effectively acting as a viable alternative to high-fidelity models, while upholding a requisite level of accuracy. ROMs can be used to predict the crack growth, given the current crack surface shape and load history [24, 25]. Ananthasayanam et al. [26] used Bayesian hybrid modeling to establish the relationship between the semi-elliptical crack size parameters and the stress intensity factor (SIF) K_I and used it for the fast prediction of in-plane crack growth. Spear et al. [27] trained a reduced-order model with an artificial neural network using parameters from discrete damage sources on the stiffened panel as inputs, with residual strength as outputs.

Constructing ROMs for predicting non-planar crack growth faces two main challenges. Firstly, crack growth evolution is a complex nonlinear process influenced by the current load and crack surface shape. Secondly, accurately representing crack surfaces parametrically is difficult due to their arbitrary spatial distribution. Presently, existing ROMs for crack growth prediction primarily focus on simple crack types or the spatial position of the crack front [5, 11, 24, 25], limiting the input range and potentially resulting in inadequate SIF predictions for non-planar cracks. Methods such as Bézier surfaces [28–30], B-spline surfaces [31–33], and NURBS surfaces [34–36], which are commonly used in the field of computer graphics, may be able to represent crack surfaces. However, even with the integration of a B-spline representation of crack geometry into the extended finite element method framework by Hectors and Waele [37], simulations still remain computationally intensive. Hence, an efficient ROM that accounts for the entire crack surface morphology in predicting non-planar crack growth is desired.

This paper introduces a novel reduced-order modeling approach for predicting non-planar crack growth that considers the shape of the crack surface. The approach's novelty lies in using a B-spline surface [38] to represent the crack surface and equidistant sampling of isoparametric nodes, resulting in a unified parameterization of the crack surface for ROM construction. This approach better captures the overall shape of the crack surface and its effect on crack growth compared to existing crack front-based methods.

The proposed method comprises two distinct stages. In the offline stage, a database featuring diverse crack surface shapes is generated through the symmetric Galerkin boundary element method - finite element method (SGBEM-FEM) coupling method [39–41]. This method effectively computes the SIFs of crack surfaces represented by B-spline techniques. Subsequently, the gathered samples undergo clustering through the K-means algorithm, and the isoparametric coordinates are transformed to a low-dimensional representation using the principal component analysis (PCA). Finally,

ROMs incorporating Gaussian process regression are trained for each cluster. In this context, the low-dimensional crack surface representation serves as the input, and the SIFs as the output. It is noteworthy that other full-order fracture mechanics simulation techniques remain applicable for the database generation, given the non-intrusive nature of the ROM construction. In the near-real-time prediction stage, the most suitable ROM is selected based on its proximity to the current crack shape. The predicted SIFs $\mathbf{K}_I$ and $\mathbf{K}_{II}$, along with the selected crack growth model, are then used to compute the increment and direction of crack growth.

The efficacy of the proposed method is demonstrated through its application to a cylindrical component reminiscent of a rotorcraft mast. The obtained results substantiate that, in comparison to the prevailing crack front curve-based reduced-order model, the proposed approach exhibits an enhanced capability to accurately predict stress intensity factors and anticipate crack growth. This efficacy emanates from the method's comprehensive consideration of the entire crack surface morphology. Furthermore, in contrast to established full-order simulation techniques, the computational efficiency of the proposed reduced-order model-based approach is remarkably elevated by three orders of magnitude. This gain in efficiency provides the method with the potential to be seamlessly integrated with Monte Carlo methods, affording a platform for conducting probabilistic crack growth analysis. This, in turn, lays the groundwork for furnishing the digital twin framework with a simulation foundation. Nonetheless, it is essential to acknowledge that the complexity inherent in the diverse forms of variation exhibited by crack surfaces in three-dimensional space presents a formidable challenge. Consequently, at this juncture, the undertaking of performing reduced-order modeling for such arbitrary non-planar crack growth patterns, with only a constrained set of training samples, remains notably intricate.

The subsequent sections of this paper are structured as follows: In Section II, we describe the crack surface representation method based on B-spline surfaces and the procedure for computing non-planar crack growth utilizing an SGBEM-FEM assembly coupling method. Section III delves into the detailed process of training the reduced-order models, encompassing the utilization of principal component analysis to diminish the dimensionality of crack surface representations, coupled with Gaussian process regression for ROM training. In Section IV, the non-planar crack growth calculated using the proposed method is compared with that obtained using the SGBEM-FEM coupling method to demonstrate the accuracy of the proposed method. Additionally, we perform a probabilistic crack growth analysis through integration with the Monte Carlo method. Finally, in Section V, we summarize our study and outline avenues for potential future exploration.

II. B-spline-based Crack Surface Representation and Automatic Generation of the Crack Database

The process of generating a crack database intended for ROM training constitutes the most time-consuming and labor-intensive phase within the offline stage. This section outlines a systematic approach aimed at achieving the automatic and efficient generation of a database tailored for non-planar cracks. The section begins with the introduction

of the representation of the non-planar crack surface through the utilization of B-spline methodology, followed by the computation of the SIF facilitated by SGBEM-FEM fracture mechanics simulation. The methodology for processing the load variations and determining the crack growth direction and increment is also discussed. All these steps are integrated into a comprehensive workflow engineered to produce a database of crack samples characterized by parametric representations and simulated SIF values.

A. B-spline-based Non-planar Crack Surface Representation

In this study, the establishment of a consistent parametric representation across a range of curved and non-uniform crack surfaces within three-dimensional models is addressed. To achieve this, the characterization of crack surfaces is undertaken through the utilization of B-spline surfaces. This approach guarantees a consistent inter-node distance along the crack front during the generation of crack surface meshes in the offline stage as well as throughout the process of crack growth in the near-real-time prediction phase. This consistency holds significance as it maintains the coherence between node coordinates and the geometric configuration of the crack surface. With regard to the crack front, the uniform spacing engenders a distinctive alignment of stress intensity factors projected by the ROMs onto the node coordinates situated along the crack front. Such a distinctive alignment, in turn, facilitates the accurate determination of both the increment and the direction of crack growth.

A B-spline surface is a mathematical representation that maps a two-dimensional parameter space (u, v) $(0 \leq u \leq 1,\ 0 \leq v \leq 1)$ onto a three-dimensional surface [34, 37]. The shape of the surface is determined by the tensor product of a set of basis functions and a collection of control points spanning three dimensions.

A knot vector, denoted as $U = \left\{u_1, u_2, \cdots, u_{n+p+1}\right\}$, is a sequence of real numbers that ascend monotonically, fulfilling the condition $u_i \in [0, 1]$ for $i = 1, 2, \cdots, n + p + 1$, where n represents the count of basis functions in the u direction and p denotes the polynomial order. The basis functions are defined by the Cox-deBoor recursive formula [34], with a piecewise constant starting when $p = 0$:

$$N_{i,0}(u) = \begin{cases} 1 & u \in [u_i, u_{i+1}] \\ 0 & otherwise \end{cases} \tag{1}$$

The i_{th} order basis function $N_{i,p}\,(u)$ with polynomial order p is obtained recursively by:

$$N_{i,p}(u) = \frac{u - u_i}{u_{i+p} - u_i} N_{i,p-1}(u) + \frac{u_{i+p+1} - u}{u_{i+p+1} - u_{i+1}} N_{i+1,p-1}(u) \tag{2}$$

Based on n basis functions $N_{i,p}\,(u)$ and their corresponding control points P_i, a B-spline curve can be obtained by

the linear combination of these basis functions:

$$C(u) = \sum_{i=1}^{n} N_{i,p}(u) P_i \tag{3}$$

Similarly, based on a two-dimensional parameter space (u, v) and a bidirectional control points grid $\boldsymbol{P}_{i,j}$, a B-spline surface with polynomial order p in the u-direction and polynomial order q in the v-direction can be obtained as:

$$S(u, v) = \sum_{i=1}^{n} \sum_{j=1}^{m} N_{i,p}(u) N_{j,q}(v) \boldsymbol{P}_{i,j} \tag{4}$$

where $N_{i,p}(u)$ and $N_{j,q}(v)$ are basis functions defined on knot vectors $U = \{u_1, u_2, \cdots, u_{n+p+1}\}$ and $V = \{v_1, v_2, \cdots, v_{m+q+1}\}$, respectively. Fig. 1 shows a typical B-spline surface $S(u, v)$ determined by a 4×3 control points grid and polynomial orders of 3 and 2 in the u and v directions, and the corresponding B-spline curves for $u = 0$ and $v = 0$ in $S(u, v)$.

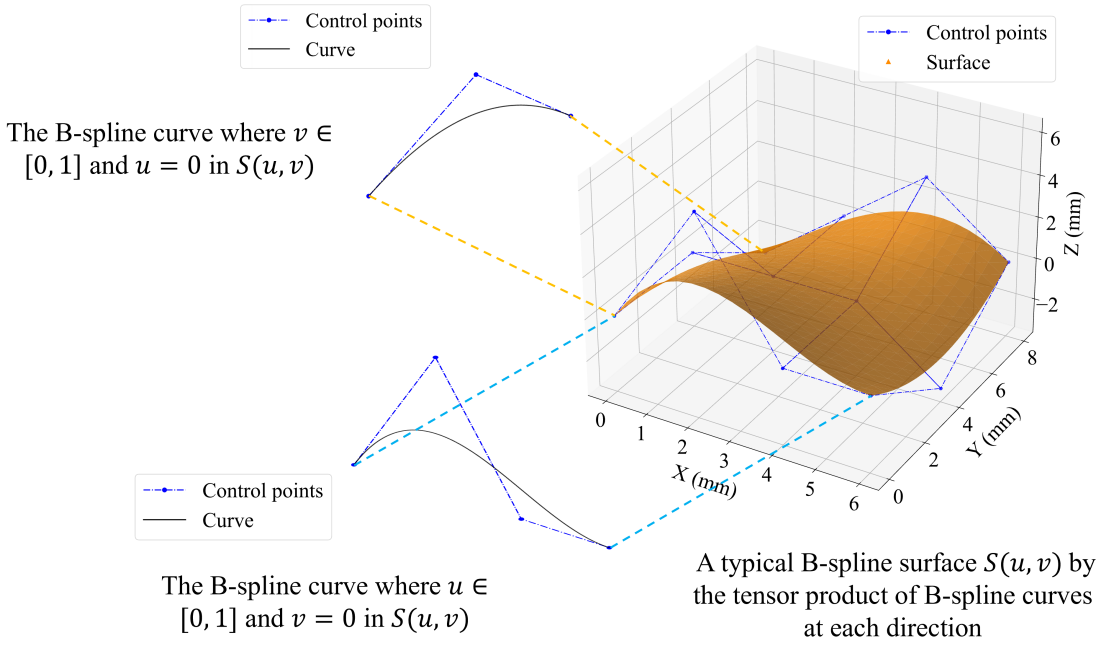

Fig. 1 A typical B-spline surface $S(u, v)$ and the corresponding B-spline curves for $u = 0$ and $v = 0$ in $S(u, v)$.

Conversely, given n data points $(D_1, D_2, \cdots, D_n)$ on a B-spline curve, the parameter u_k corresponding to the k_{th} data point D_k can be obtained using various techniques, including the uniformly spaced method, the chord length method, or the centripetal method. To illustrate, the centripetal method can be employed to compute the parameter as

outlined below:

$$u_1 = 0 \tag{5}$$

$$u_k = \frac{\sum_{i=1}^{k-1} |D_{i+1} - D_i|^a}{\sum_{i=1}^{n-1} |D_{i+1} - D_i|^a} \ (k = 2, 3, \cdots, n-1) \tag{6}$$

$$u_n = 1 \tag{7}$$

where the exponent value a is typically chosen to be 0.5.

Combined with Eq. (3), the following equation can be obtained:

$$D_k = C(u_k) = \sum_{i=1}^{n} N_{i,p}(u_k) P_i \quad (k = 1, 2, \cdots, n) \tag{8}$$

With D_k and $N_{i,p}(u_k)$ being known, and $P_1, P_2, \cdots, P_n$ derivable through matrix operations, a B-spline curve can be sequentially determined, encompassing all these data points, based on the provided data points $(D_1, D_2, \cdots, D_n)$ and the polynomial order p. In a similar vein, when confronted with a grid consisting of $(n+1) \times (m+1)$ data points across a surface, as well as specific polynomial orders (p, q), an analogous approach can be employed to ascertain a B-spline surface that sequentially passes through all the designated data points in the given order employing the similar methods [34, 38].

B. A Rotorcraft-mast-type Structure and Its Multiaxial Load Profile

In order to comprehensively elucidate the proposed methodology, a two-radius hollow cylindrical component is adopted as an example. This component bears resemblance to a rotorcraft mast presented in [11]. The material properties and geometric properties of the component are detailed in Table 1 and Table 2, respectively. The fillet area of the component is assumed to contain a pre-defined circular crack with a radius of 1.27 mm. The uncracked structure and the crack surface were discretized into finite elements using MSC/Patran, as illustrated in Fig. 2. In the context of the crack surface, the predefined initial crack is manifested as a flat circular region, with the surrounding annular region denoting the area of crack growth.

Table 1 Material properties

Aluminum 7075-T6	
Modulus of elasticity (E)	72 GPa
Poisson ratio (ν)	0.32
Yield stress (σ_s)	450 MPa
Ultimate stress (σ_b)	510 MPa

Five different combinations of bending moment and torque are assumed to simulate the multiaxial load borne by the

Table 2 Geometric properties

Cylinder properties	
Length	152 mm
Inside radius	7.62 mm
Thicker outside radius	20.3 mm
Thinner outside radius	15.24 mm

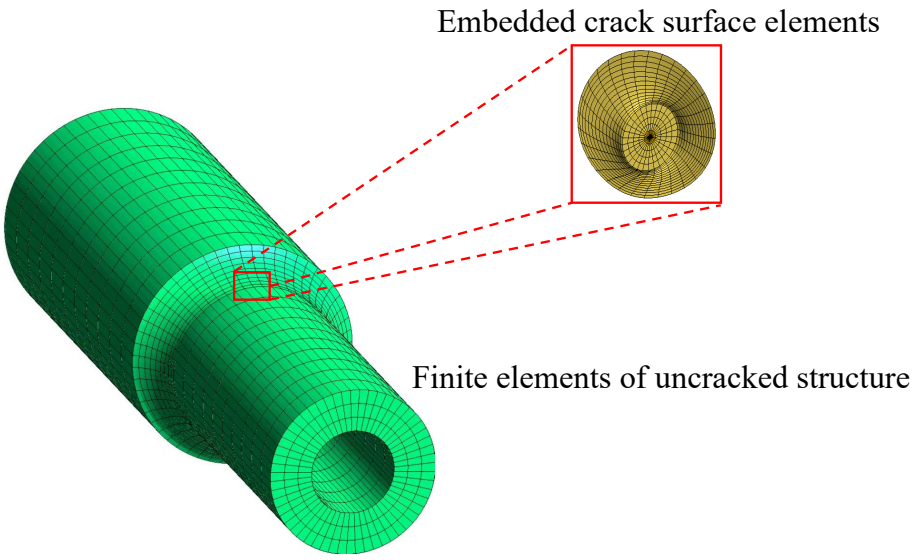

Fig. 2 Meshes of the uncracked structure and crack surface.

component during service, as listed in Table 3. For multiple rotorcraft of the same type, the courses of these bending moments and torques are different due to their mission variations. Table 4 shows 15 different bending moment and torque histories. Each load history includes 8 load blocks, which are randomly sampled from the 5 possible bending moment and torque combinations listed in Table 3. An appropriate number of cycles is set for each load block to ensure that the crack growth reaches a sufficient level after experiencing that load block. A typical case of load history 12 is shown in Fig. 3.

Table 3 Description of bending moment and torque

Load type	Bending moment ($N \cdot m$)	Torque ($N \cdot m$)
1	198	395
2	226	282
3	254	169
4	282	56
5	282	395

Table 4 Different load histories

Load history	Load type							
1	3	4	5	5	5	4	2	2
2	5	5	4	3	2	2	2	1
3	5	5	1	4	3	3	1	5
4	4	1	2	2	4	1	3	1
5	4	4	4	5	3	1	4	5
6	4	2	5	4	5	1	2	5
7	5	5	3	2	5	3	2	5
8	3	2	3	5	4	4	5	5
9	4	5	3	3	1	3	5	2
10	3	1	1	4	5	4	5	3
11	5	2	1	2	1	3	1	4
12	2	3	4	2	2	1	4	4
13	5	4	3	3	4	2	4	2
14	3	4	2	4	4	1	4	3
15	5	5	2	1	5	1	5	2

C. Isoparametric representation of the crack surface

In this study, the B-spline surface, as described in Section II.A, is utilized to represent the annular region encircling the initial circular crack, which is the locus of subsequent crack growth. The radial and circumferential directions of the annular surface are denoted as u and v, respectively, as illustrated in Fig. 4a. The polynomial orders for the u and v directions are set to 1 and 3, respectively. The corner nodes and circumferential middle nodes of the elements are recognized as known data points on the surface, as visually indicated in Fig. 4b.

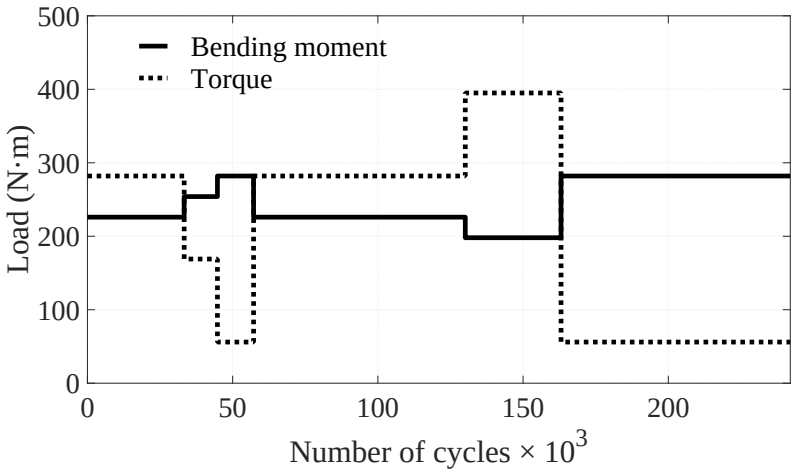

Fig. 3 A typical load history.

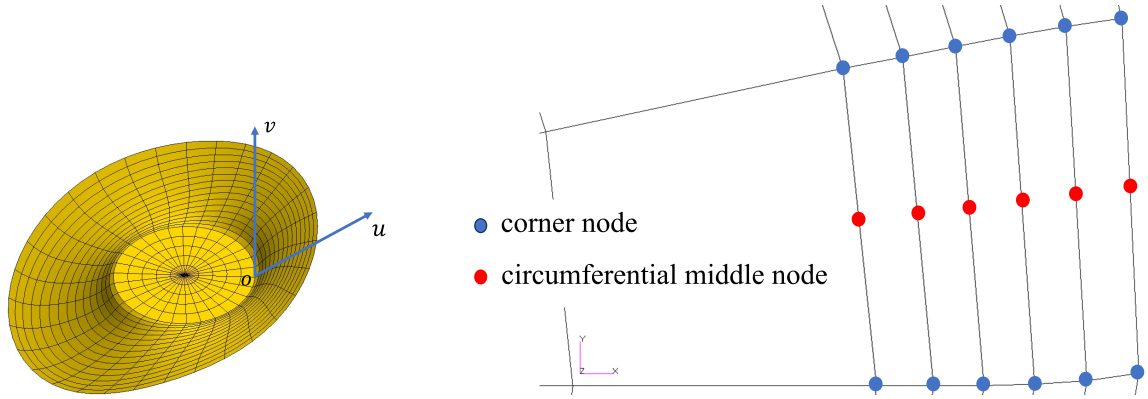

(a) Setting of u and v directions of an annular surface.

(b) Setting of known data points.

Fig. 4 Settings of orientations and known data points for an annular surface.

Using these designated data points and the polynomial orders defined in both directions, the B-spline representation of the surface is established by employing the open-source modeling framework NURBS-Python [38]. Subsequently, isoparametric nodes are uniformly sampled on the B-spline surface, adhering to the u and v directions. Assuming that the annular surface is divided into N elements in the circumferential direction, for the k_{th} crack growth, the known data points are arranged into a grid of $(k+1) \times 2N$, where $k+1$ and $2N$ are the number of data points corresponding to the u direction and v direction, respectively. All the combination of elements (u_i, v_j) from sets $U = \{0, \frac{1}{k}, \frac{2}{k}, \cdots, 1\}$ and $V = \{0, \frac{1}{2N-1}, \frac{2}{2N-1}, \cdots, 1\}$ are substituted into the obtained B-spline surface $S(u, v)$. Consequently, a uniform representation of the crack surface, possessing $(k+1) \times 2N$ isoparametric nodes, is attained.

D. SGBEM-FEM Coupling Simulation and Linear Superposition to Calculate the Stress Intensity Factor

To create a fracture mechanics database, an effective simulation method, the SGBEM super element-FEM coupling method, has been adopted in this study. This method involves the direct assembly of an SGBEM "super element", characterizing a local subdomain encompassing arbitrary cracks, with the finite elements representing an uncracked structure, facilitated by a stiffness matrix. The SGBEM employed to model the local crack subdomain exhibits a remarkable capacity to accurately capture the stress and strain singularities present at the crack front. This method further permits the utilization of coarser finite element meshes for most regions without cracks and obviates the need for intricate mesh subdivisions in proximity to the crack front. One noteworthy advantage of this approach lies in the separation of the modeling tasks between FEM and SGBEM models, necessitating only a single FEM model. This division enables a concentrated focus on modeling crack samples of varied shapes. However, it's essential to acknowledge that alternative full-order fracture mechanics simulation techniques can be applied for the purpose of generating the database, considering the non-intrusive nature of ROM construction.

To facilitate the creation of crack surface meshes, the isoparametric B-Spline representation of the crack surface is exported as a stereolithography (STL) file. This file format can subsequently be imported into MSC/Patran for the purpose of mesh generation. The corner nodes and middle nodes of the outermost elements are aligned with the isoparametric nodes along the front curve of the B-Spline crack surface, that is, $S(u_i, v_j)$ with $u_i = 1$ and $v_j = 0, \frac{1}{2N-1}, \frac{2}{2N-1}, \cdots, 1$, through the method of editing elements. Fig. 5 visually delineates the progression of generating crack surface elements with uniformly distributed front edge nodes within MSC/Patran. This is achieved starting from the known data points, which are not inherently uniformly distributed.

The generated crack surface elements and the finite element model of the uncracked structure are input into the SGBEM-FEM coupling program, which allows for the calculation of K_I and K_{II} at each isoparametric node on the crack front. The procedural workflow is graphically presented in Fig. 6, and its essence can be succinctly summarized as follows:

1) Partition the finite elements of the uncracked structure.

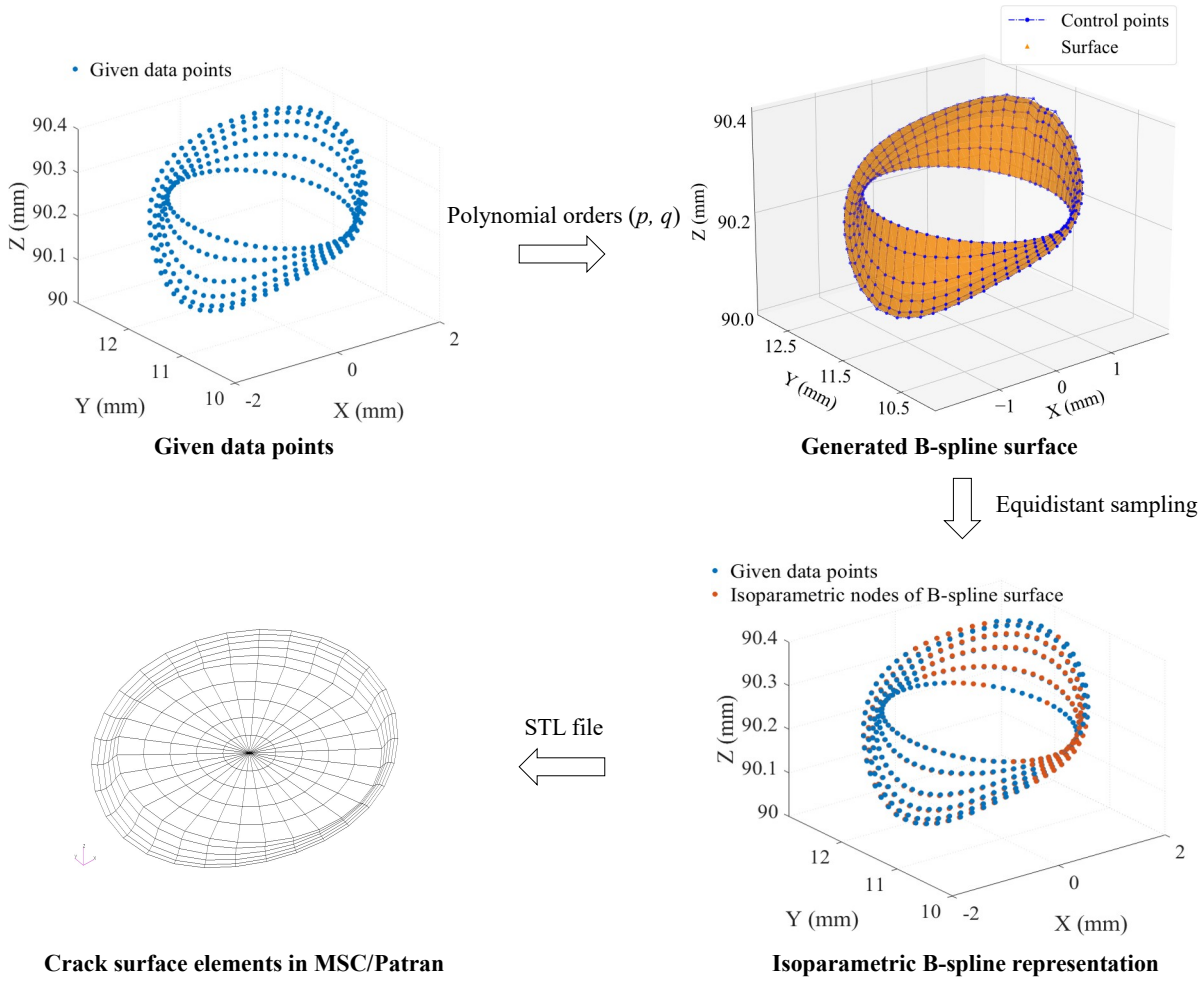

Fig. 5 The formation process of crack surface elements with uniformly distributed front edge nodes.

2) Isolate the finite elements of the localized region near the crack.

3) Eliminate internal nodes from the extracted finite elements, reconstructing them into two-dimensional boundary elements featuring exclusively external surfaces.

4) Integrate the generated two-dimensional boundary elements and crack surface elements in accordance with the actual crack position within the structure. These components collectively constitute the SGBEM super element.

5) Assemble the super element and the uncracked structure's finite elements via the stiffness matrix, creating an analytical model to which fatigue loads are applied for fracture analysis.

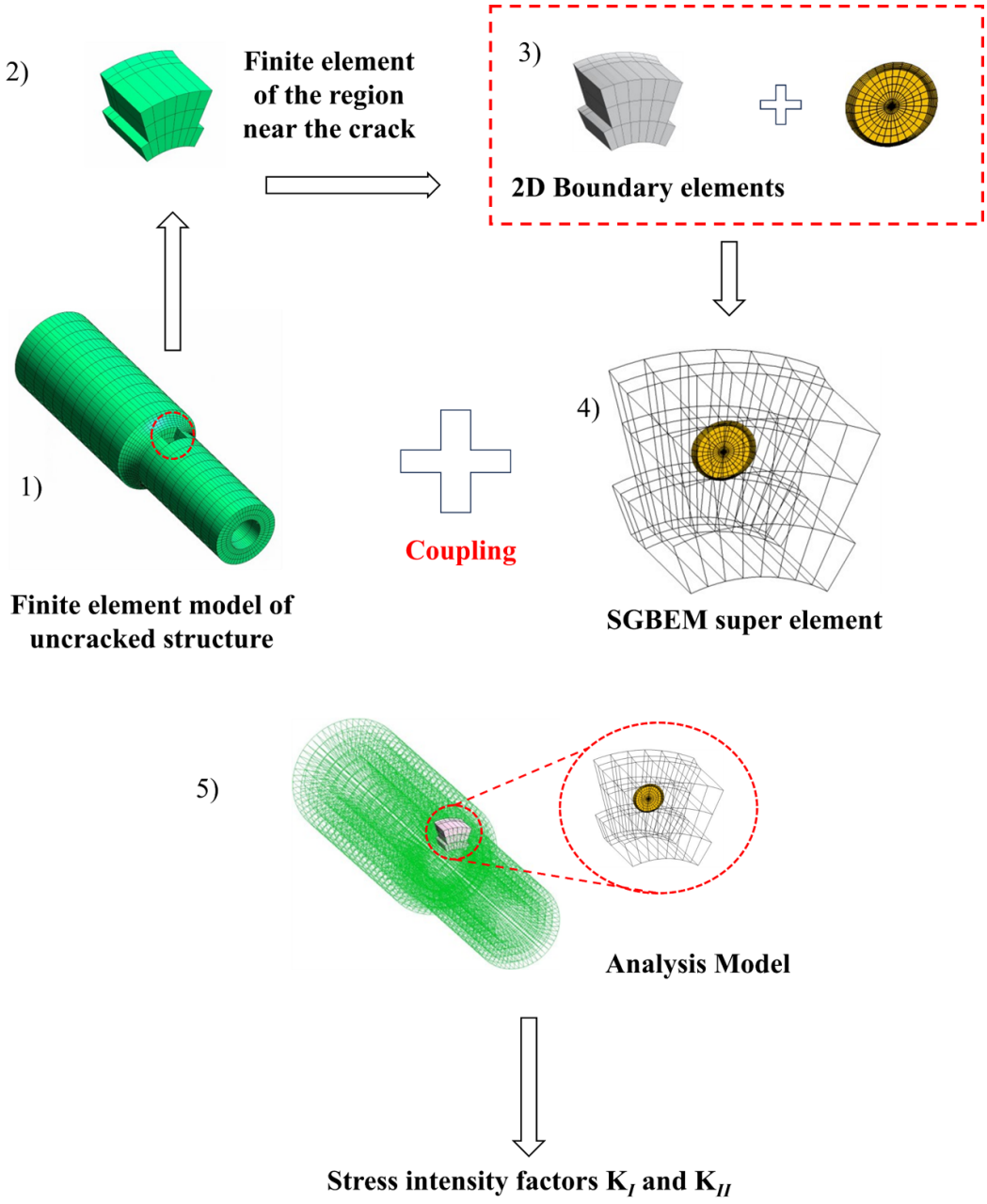

Fig. 6 Calculation of stress intensity factors based on the SGBEM-FEM coupling method.

An essential consideration pertains to the influence of load variations on the simulation outcomes. Previous scholarly endeavors have delved into the incorporation of bending moment and torque as inputs to ROMs for the prognosis of crack growth [11]. However, it is noteworthy that, in the realm of linear elastic fracture mechanics, the SIFs maintain linear proportionality to the applied loads. This characteristic renders it feasible to disentangle the load factor from the SIF calculations, thereby bolstering the precision and efficiency of the ROM training procedure. In our study, we embrace the benchmark load method [5] as the basis for SIF computation. As both K_I and K_{II} are linearly related to the bending moment or torque, K_I and K_{II} under any bending moment B and torque T can be obtained by the linear superposition principle:

$$K_I = K_{I,B_{base}} \frac{B}{B_{base}} + K_{I,T_{base}} \frac{T}{T_{base}} \tag{9}$$

$$K_{II} = K_{II,B_{base}} \frac{B}{B_{base}} + K_{II,T_{base}} \frac{T}{T_{base}} \tag{10}$$

where B_{base} and T_{base} are benchmark loads for bending moment and torque, respectively, which are set as the maximum values $282\,N \cdot m$ and $395\,N \cdot m$ in Table 3. $K_{I,B_{base}}$, $K_{II,B_{base}}$, $K_{I,T_{base}}$ and $K_{II,T_{base}}$ are SIFs calculated under the benchmark loads. In the subsequent crack growth calculation, the reference loads B_{base} and T_{base} are applied to the finite element model representing the uncracked structure, and then K_I and K_{II} under the current bending moment B and torque T are calculated according to Eqs. (9)-(10).

E. Determination of the Non-planar Crack Growth Direction and Rate

In this paper, the maximum tangential stress criterion [42, 43] is adopted to determine the direction of crack growth. For determining the magnitude of crack growth increment, a modified Paris law [43] with specific parameters $C = 6.54E-13$ and $m = 3.8863$ is adopted. An inherent advantage of the proposed approach lies in its direct prediction of SIFs as opposed to forecasting the subsequent crack location. This feature renders seamless integration with other criteria governing crack growth direction and models pertinent to crack growth, making it adaptable to real-world contexts.

The crack growth angle α and rate $\frac{da}{dN}$ can be determined using the formulations as follows:

$$\alpha = \text{sign}\left(-K_{II}\right) \cos^{-1}\left(\frac{3K_{II}^2 + \sqrt{K_I^4 + 8K_I^2K_{II}^2}}{K_I^2 + 9K_{II}^2}\right) \tag{11}$$

$$K_{eff} = \left(K_I^4 + 8K_{II}^4\right)^{1/4} \tag{12}$$

$$\frac{da}{dN} = C\left(\Delta K_{eff}\right)^m \tag{13}$$

To enhance the efficiency of the calculations while ensuring accuracy, the crack growth increment is calculated by

$\Delta \boldsymbol{a} = d_k \frac{d\boldsymbol{a}}{dN}$, where d_k is the load block increment defined by the user [11].

In order to calculate the subsequent crack growth, a transformation from the local coordinate system to the global coordinate system is required. The local coordinate system is defined by the unit vectors $\boldsymbol{t}_{cf}$, $\boldsymbol{n}_{cf}$, and $\boldsymbol{n}_{cs}$ [37], where $\boldsymbol{t}_{cf}$ is the unit vector tangent to the front edge of the crack, $\boldsymbol{n}_{cf}$ is the unit vector normal to the crack front and tangent to the crack surface, and $\boldsymbol{n}_{cs}$ is the unit binormal vector normal to the crack surface, as shown in Fig. 7. In the local coordinate system, the increment at one node is expressed as $\Delta \boldsymbol{a}_{local} = [0 \; da \cdot \cos\alpha \; da \cdot \sin\alpha]$.

For the i_{th} isoparametric node, the corresponding $\boldsymbol{t}_{cf,i}$ and $\boldsymbol{n}_{cf,i}$ can be obtained by finding the first partial derivative of the surface equation $S(u, v)$ (According to the setting, $u_i = 1, v_i = \frac{i-1}{2N-1}$ at the i_{th} isoparametric node at the crack front):

$$\boldsymbol{n}_{cf,i} = \frac{\frac{\partial}{\partial u} S(u,v)\Big|_{u=1, v=\frac{i-1}{2N-1}}}{\left|\frac{\partial}{\partial u} S(u,v)\Big|_{u=1, v=\frac{i-1}{2N-1}}\right|} \tag{14}$$

$$\boldsymbol{t}_{cf,i} = \frac{\frac{\partial}{\partial v} S(u,v)\Big|_{u=1, v=\frac{i-1}{2N-1}}}{\left|\frac{\partial}{\partial v} S(u,v)\Big|_{u=1, v=\frac{i-1}{2N-1}}\right|} \tag{15}$$

The corresponding binormal vector $\boldsymbol{n}_{cs,i}$ then be obtained by:

$$\boldsymbol{n}_{cs,i} = \frac{\boldsymbol{n}_{cf,i} \times \boldsymbol{t}_{cf,i}}{\left|\boldsymbol{n}_{cf,i} \times \boldsymbol{t}_{cf,i}\right|} \tag{16}$$

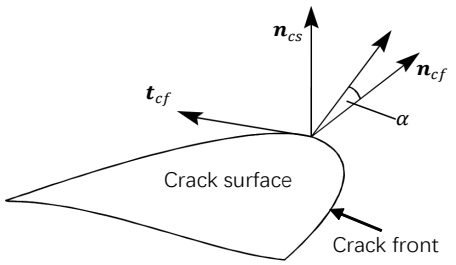

Fig. 7 Local coordinate system at the crack front.

The global coordinate system is expressed as $(\boldsymbol{e}_1, \boldsymbol{e}_2, \boldsymbol{e}_3)$, and the crack growth increment is transformed to the global coordinate system by:

$$\Delta \boldsymbol{a}_{global} = \Delta \boldsymbol{a}_{local} \cdot \begin{bmatrix} \boldsymbol{t}_{cf} \cdot \boldsymbol{e}_1 & \boldsymbol{t}_{cf} \cdot \boldsymbol{e}_2 & \boldsymbol{t}_{cf} \cdot \boldsymbol{e}_3 \\ \boldsymbol{n}_{cf} \cdot \boldsymbol{e}_1 & \boldsymbol{n}_{cf} \cdot \boldsymbol{e}_2 & \boldsymbol{n}_{cf} \cdot \boldsymbol{e}_3 \\ \boldsymbol{n}_{cs} \cdot \boldsymbol{e}_1 & \boldsymbol{n}_{cs} \cdot \boldsymbol{e}_2 & \boldsymbol{n}_{cs} \cdot \boldsymbol{e}_3 \end{bmatrix} \tag{17}$$

F. Workflow of the Crack Database Generation

Due to the diverse variations of crack surfaces in 3D space, implementing the parametric sampling method to generate crack samples [5] is difficult. Therefore, in this study, samples are generated through multiple complete crack growth simulations by pre-defining the variations in the load spectrum. The flow chart of the entire process of non-planar crack growth is depicted in Fig. 8.

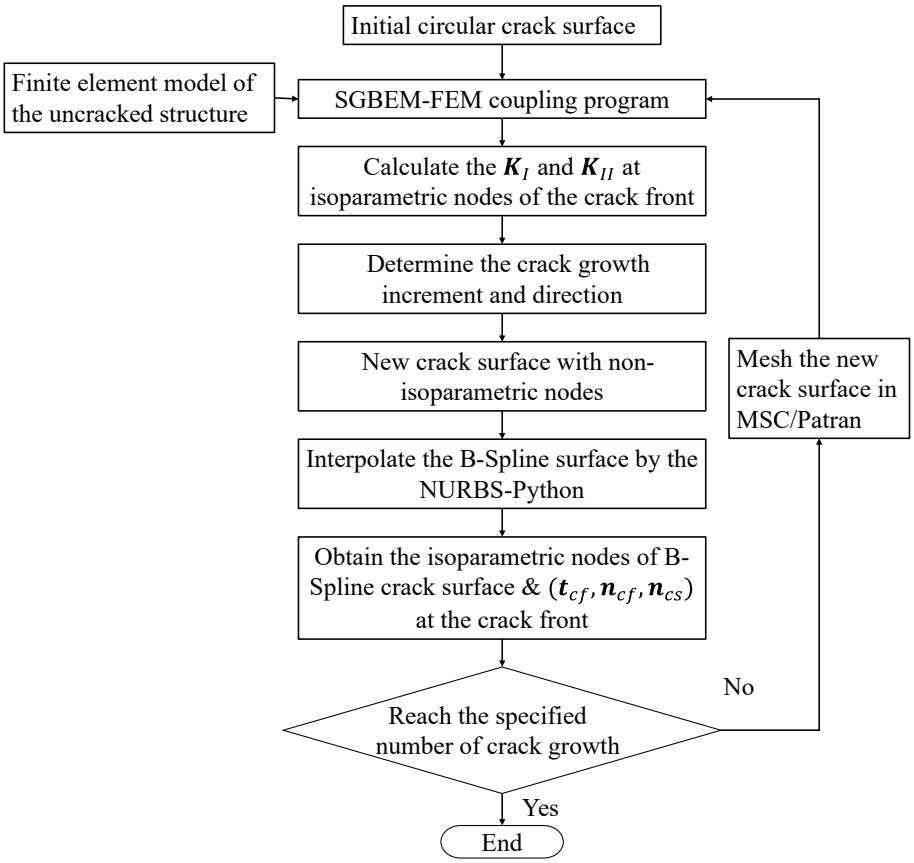

Fig. 8 The flowchart of the full-order simulation of the non-planar crack growth based on B-spline surface representation.

Starting from the initial crack represented by an isoparametric representation, the SGBEM-FEM coupling program is invoked to simulate the SIFs $\mathbf{K}_I$ and $\mathbf{K}_{II}$. The SIFs are then utilized to generate the crack growth direction and increment, as described in Section II.E. The local coordinate systems are calculated, and the coordinates of new nodes generated by crack growth are added to the previous crack surface, creating a new surface. Subsequently, this freshly created surface is subjected to interpolation, which involves B-Spline surface interpolation, culminating in the establishment of an updated isoparametric representation. This updated representation, in turn, is harnessed to generate an augmented crack surface model, priming it for the forthcoming fracture mechanics simulation. This iterative process continues until the predetermined count of crack growth increments has been achieved.

By altering the number of cycles per load type, each load history listed in Table 4 can be utilized to calculate

different crack growth histories, each containing 7 crack surfaces. All the crack surfaces, along with their isoparametric coordinates and the calculated $\mathbf{K}_I$ and $\mathbf{K}_{II}$, were then used for the training of the ROMs.

III. ROMs training for fracture mechanics parameter prediction

In this section, the ROMs designed to forecast the SIFs along the crack front are formulated, utilizing the crack database created in the preceding section. The ROMs take as input the isoparametric coordinates of the B-Spline crack surface and yield as output the $\mathbf{K}_I$ and $\mathbf{K}_{II}$ values at the isoparametric nodes situated along the crack front. With due regard to both bending and torque loads and encompassing two distinct SIF categories, a total of four distinct ROMs are established. These models are mathematically expressed as follows:

$$\mathbf{K}_{I,B_{base}} = \mathcal{M}_{I,B_{base}}(\boldsymbol{C}) \tag{18}$$

$$\mathbf{K}_{I,T_{base}} = \mathcal{M}_{I,T_{base}}(\boldsymbol{C}) \tag{19}$$

$$\mathbf{K}_{II,B_{base}} = \mathcal{M}_{II,B_{base}}(\boldsymbol{C}) \tag{20}$$

$$\mathbf{K}_{II,T_{base}} = \mathcal{M}_{II,T_{base}}(\boldsymbol{C}) \tag{21}$$

where $\mathbf{K}_{I,B_{base}}$, $\mathbf{K}_{I,T_{base}}$, $\mathbf{K}_{II,B_{base}}$, $\mathbf{K}_{II,T_{base}}$ represent the reference values of the SIFs under benchmark loads B_{base} and T_{base}, $\mathcal{M}_{I,B_{base}}$, $\mathcal{M}_{I,T_{base}}$, $\mathcal{M}_{II,B_{base}}$, $\mathcal{M}_{II,T_{base}}$ represent the corresponding ROMs, respectively, $\boldsymbol{C}$ represents the isoparametric coordinates of the crack surface.

The process of constructing the ROMs involves three steps: division of samples using clustering algorithms, reduction of input dimensionality through principal component analysis, and training of surrogate models via Gaussian process regression.

Given that the samples in the database may not be uniformly distributed in the parameter space, as shown in Fig. 9, the K-means algorithm, a widely used clustering method, as described in Hartigan and Wong [44] is adopted here. The configuration stipulates the generation of 12 clusters, with a cap of 500 rounds for the maximum number of iterations across all crack samples. Further discourse concerning the particulars of the clustering algorithm's configuration is available in the Appendix. In the stage of near-real-time prediction, the distance between the current crack surface and the mean vector pertaining to each cluster is computed. Subsequently, the cluster exhibiting the minimal distance is selected, signifying its compatibility with the current crack surface. The trained ROMs associated with that cluster are then used to predict the fracture mechanics parameters of the crack surface.

Although the crack surface can be characterized by the isoparametric nodes based on B-spline surfaces, using them directly as inputs to the ROMs would greatly increase the training burden due to the large number of nodes. To mitigate this, PCA is used to project the coordinates of these isoparametric nodes into a lower-dimensional latent space. In this

paper, the retained variance should not be less than 99.99% when using PCA for projection. Additionally, facilitated by PCA, we present in Fig. 9 the depiction of classes generated through the K-means clustering algorithm, within a two-dimensional latent space formed by the first two principal components. Distinct classes are discernible by virtue of distinct colors. Evidently, the K-means algorithm classifies all samples into various clusters, drawing upon the spatial distribution of the sample coordinates.

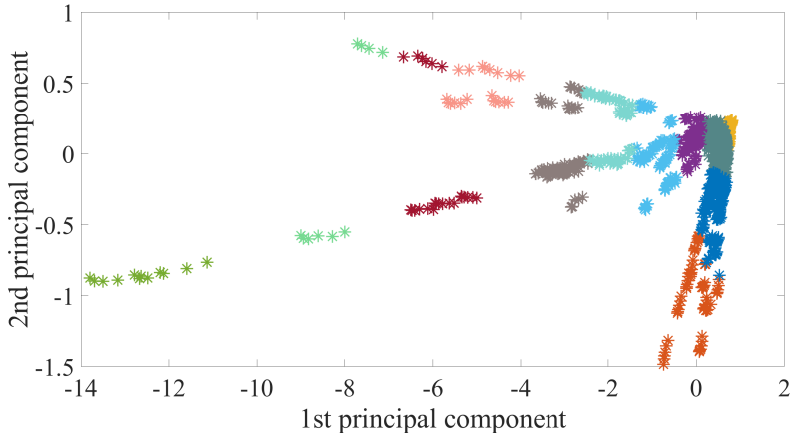

Fig. 9 Clustering by K-means algorithm (Displayed in two-dimensional PCA latent space).

The Gaussian process regression [45, 46] is used as the regression method for training ROMs. In this context, the mean function is established as zero, while the covariance function adopts the form of a squared exponential covariance function. The likelihood function is configured as a Gaussian likelihood function, and the inference method pertains to regression under the Gaussian likelihood. These parameter settings have been subjected to verification, affirming their capacity to yield the requisite training precision. The corresponding coordinates of the crack surface in the latent space are used as the input of the ROMs, and the output is $\mathbf{K}_I$ and $\mathbf{K}_{II}$ at the front edges.

According to the 75%/25% division principle, a designated number of samples is randomly chosen from each class, and the selected samples constitute the training set. Conversely, the remaining samples form the test set, thereby enabling the training of the ROMs. The errors are defined as follows (relative error is not used for K_{II} due to the proximity of some values to zero, potentially yielding extremely large relative errors and a loss of reference values):

$$\varepsilon_{K_I} = \frac{1}{q \times N_s} \sum_{i=1}^{q} \sum_{j=1}^{N_s} \frac{\left|\mathbf{y}_{ij} - \hat{\mathbf{y}}_{ij}\right|}{\mathbf{y}_{ij}} \tag{22}$$

$$\varepsilon_{K_{II}} = \frac{1}{q \times N_s} \sum_{i=1}^{q} \sum_{j=1}^{N_s} \left|\mathbf{y}_{ij} - \hat{\mathbf{y}}_{ij}\right| \tag{23}$$

where N_s is the number of samples in the test set, q is the number of isoparametric nodes of the crack front, $\mathbf{y}$ represents

the results calculated by the SGBEM-FEM coupling program, and $\hat{\mathbf{y}}$ is the corresponding result predicted by the ROMs. The errors for each cluster are summarized in Table 5.

Table 5 Summary of test errors for stress intensity factor prediction using the ROMs

Cluster number	The number of samples	$\varepsilon_{K_I}(\%)$	$\varepsilon_{K_{II}}(MPa\sqrt{m})$
1	261	0.77	0.0334
2	10	6.15	0.3052
3	69	3.71	0.1273
4	12	1.16	0.0454
5	22	6.01	0.3790
6	375	3.73	0.2553
7	97	1.77	0.1209
8	85	1.03	0.0425
9	118	1.93	0.1822
10	40	2.34	0.1190
11	629	1.86	0.0849
12	67	0.37	0.0230

The accuracy of the ROMs was compared for cases both with and without K-means clustering of the crack database. In the case without clustering, 1339 samples were randomly selected from the crack database as the training set, with the remaining 446 samples used as the test set. The resulting errors for K_I and K_{II} were 9.94% and $0.4173MPa\sqrt{m}$, respectively. Evidently, these errors are demonstrably larger than the outcomes attained through the use of clustered samples. The predictions of the fracture mechanics parameters for a new crack surface not included in the above training and test sets were compared, as shown in Fig. 10. The results indicate that the K-means algorithm effectively clusters the samples based on their spatial coordinates and results in more consistent predictions compared to the case without clustering. Furthermore, the ROMs based on the crack surface, which consider the spatial position of the crack surface, are seen to provide more accurate predictions compared to the ROMs based on the crack front curve, which is also shown in Fig. 10.

The computational efficiency of the proposed ROM-based method is compared with that of the full-order simulation by evaluating the average time required to calculate $\mathbf{K}_I$ and $\mathbf{K}_{II}$ of each crack class. The results are shown in Fig. 11, which demonstrate the significantly reduced computational time of the ROM-based method. The average time to call the ROMs, which is approximately 1.3 seconds, is three orders of magnitude more efficient than directly using the SGBEM-FEM coupling program (full-order model). The calculations were performed on a desktop equipped with an Intel Core i7-6700 processor and 32 GB of memory.

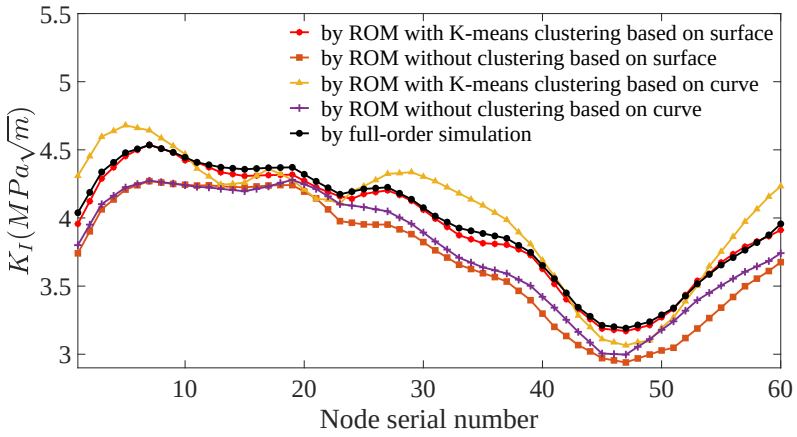

(a) K_I

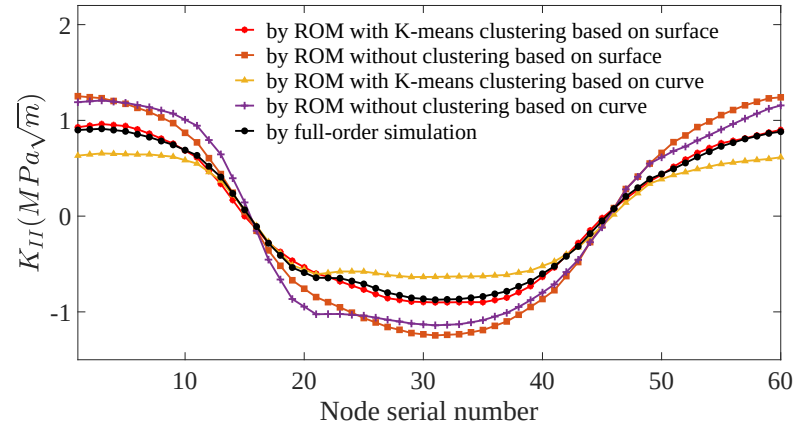

(b) K_{II}

Fig. 10 Comparison of the K_I and K_{II} prediction: full-order and reduced-order, with and without clustering, surface-based and curve-based methods.

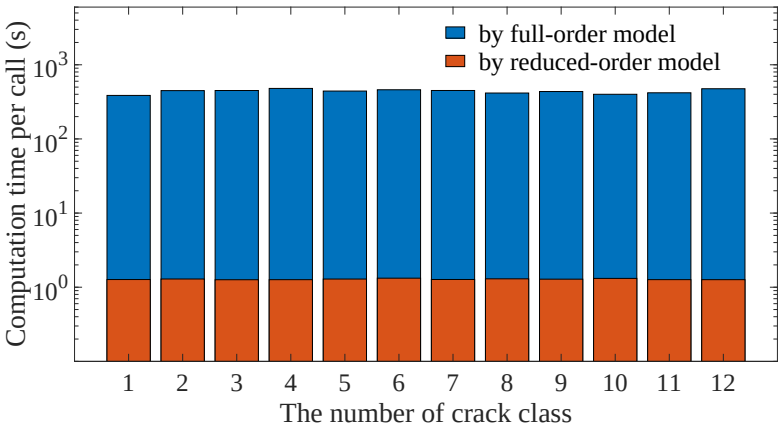

Fig. 11 Comparison of the average computation time per call between the SGBEM-FEM assembly coupling program and ROMs.

IV. Near-Real-Time Non-Planar Crack Growth Prediction Using Reduced-Order Models

In this section, the utilization of the constructed ROMs for online crack growth prediction is elucidated. The initial emphasis is directed towards deterministic, near-real-time predictions of crack growth. Following this, the discussion delves into the presentation of a Monte Carlo-based probabilistic crack growth analysis. This demonstration showcases the proposed approach's capacity for seamless integration into the digital twin framework.

A. Deterministic Near-Real-Time Crack Growth Prediction Based on ROMs

The process of deterministic crack growth prediction is elucidated in detail, followed by a depiction of the workflow.

The methodology for near-real-time prediction of crack growth using ROMs is outlined as follows: The crack growth of the initial circular crack (i.e., the first instance of crack growth) is determined by utilizing the pre-calculated $\mathbf{K}_I$ and $\mathbf{K}_{II}$ values. In subsequent crack growth scenarios, the existing nodes and polynomial orders within the u and v directions are utilized for B-Spline surface interpolation. This interpolation produces isoparametric nodes and $(\boldsymbol{t}_{cf}, \boldsymbol{n}_{cf}, \boldsymbol{n}_{cs})$ values for each node along the crack front. The distance between the generated isoparametric node coordinates and the mean vector of each crack cluster is computed, leading to the identification of the cluster that best corresponds to the current crack surface. Then, the corresponding pre-trained ROMs are used to predict $\mathbf{K}_I$ and $\mathbf{K}_{II}$ of the crack surface, and the crack growth direction and increment are determined. The flowchart for near-real-time prediction of crack growth is depicted in Fig. 12.

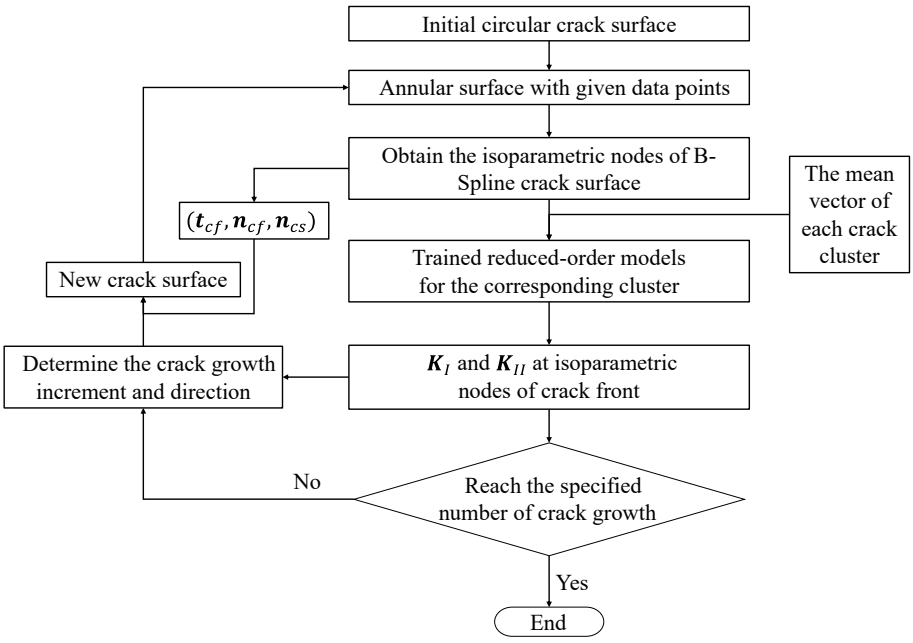

Fig. 12 Flow chart for the near-real-time crack growth prediction.

The efficacy of the proposed method is demonstrated through a comparative analysis between the results obtained from full-order simulations and the reduced-order model-based approach introduced in this study. To achieve this, five

new crack growth histories are selected randomly from the load histories listed in Table 4 with different numbers of cycles for each load type, which differ from the existing crack growth histories discussed in Section II. The evolution of the crack front corresponding to these five distinct growth histories is computed using the SGBEM-FEM coupling program in full-order simulation. Subsequently, the outcomes of the full-order simulations are contrasted with those generated by the reduced-order model-based approach proposed in this paper. The comparison outcomes are presented in Fig. 13.

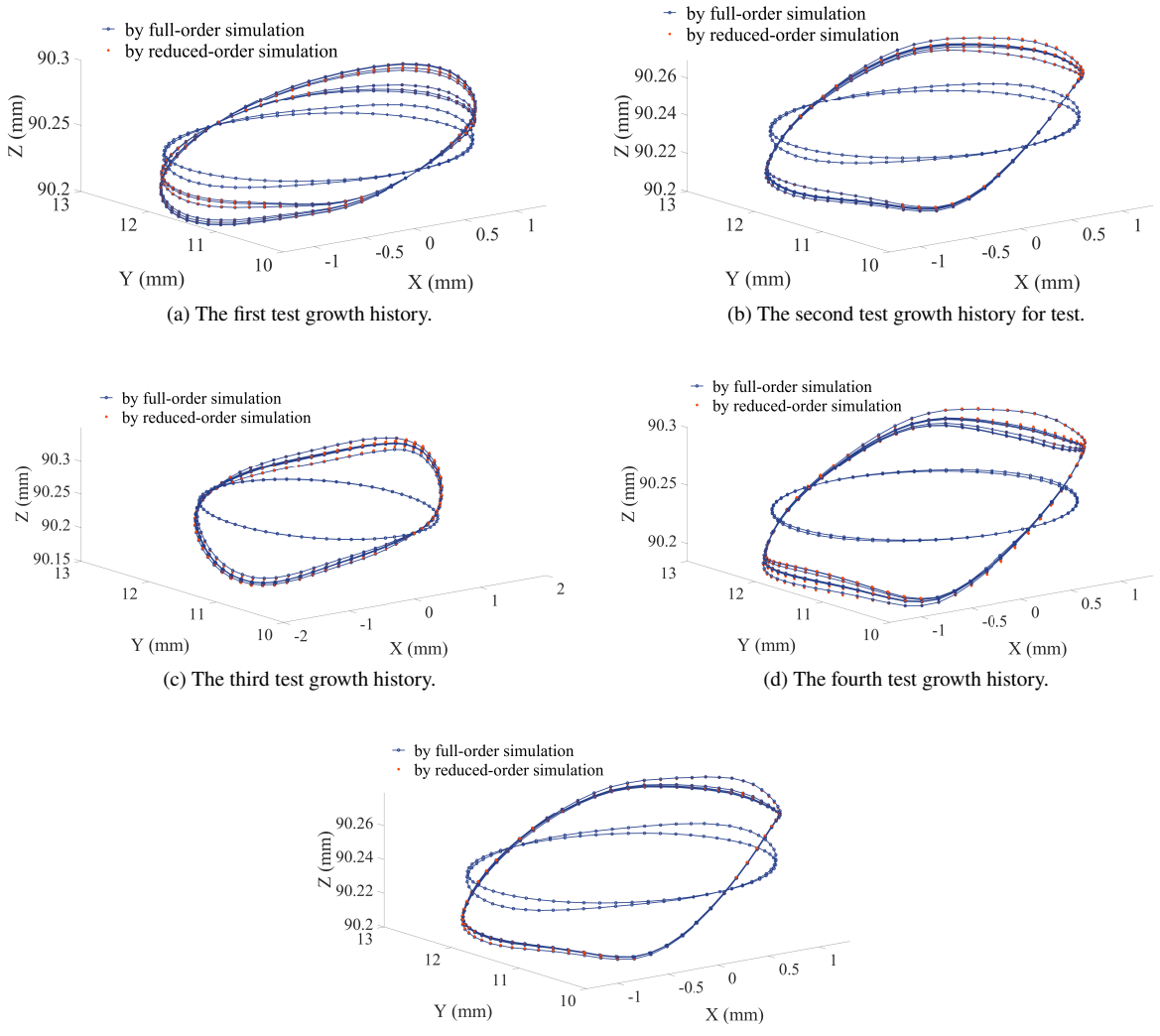

(a) The first test growth history.

(b) The second test growth history for test.

(c) The third test growth history.

(d) The fourth test growth history.

(e) The fifth test growth history.

Fig. 13 Comparison of non-planar crack growth predicted by the proposed reduced-order model and full-order SGBEM-FEM coupling simulation.

The error of each growth history for testing calculated by the ROMs is determined by:

$$e_k^d = \frac{1}{N_p} \sum_{i=1}^{N_p} \left\| \boldsymbol{C}_{i,k} - \widehat{\boldsymbol{C}}_{i,k} \right\|_2 \quad (k = 1, 2, \cdots, 5) \tag{24}$$

where N_p denotes the number of data points on the annular surface, k denotes the k_{th} growth history for the test, $\boldsymbol{C}$ denotes node coordinates calculated by the SGBEM-FEM assembly coupling program, and $\widehat{\boldsymbol{C}}$ denotes corresponding node coordinates calculated by the proposed method in this paper.

In addition, the crack surface angle error is quantified using the crack surface angle θ [47]. This angle is defined as the included angle between the vectors $\boldsymbol{n}_{cf}$ at the same isoparametric nodes between the final and initial crack surfaces, as shown in Fig. 14. The computed outcomes for the first growth history in the test are illustrated in Fig. 15. The error associated with the calculated crack surface angle is defined as follows:

$$e_k^{\theta} = \frac{1}{N_f} \sum_{i=1}^{N_f} \left| \theta_{i,k}^{FOM} - \theta_{i,k}^{ROM} \right| \quad (k = 1, 2, \cdots, 5) \tag{25}$$

where N_f represents the number of isoparametric nodes at the crack front, and θ^{FOM} and θ^{ROM} denote the crack surface angles obtained by the full-order model and reduced-order model, respectively.

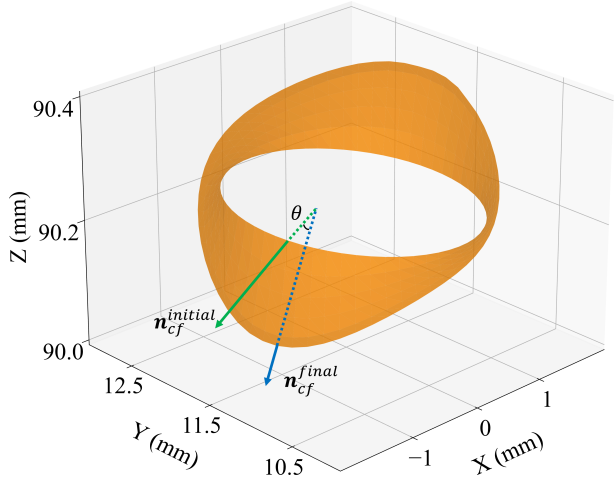

Fig. 14 Schematic diagram of crack surface angle θ.

Table 6 provides a summary of the error for each growth history in the test. The values of e^d and e^{θ} for the third growth history exhibit relatively higher errors. This discrepancy can be attributed to the circumstance where the number of cycles in the second crack growth for this particular history extends beyond the range covered by the corresponding values in the training set. However, it's important to highlight that these results remain within an acceptable realm of accuracy. In addition, the prediction results of the ROMs based on the crack front curve are also listed in Table 6. Notably, the surface-based ROM, which comprehensively incorporates the spatial disposition of the complete crack surface, yields more precise predictions than those predicated solely on the front curve.

Moreover, to test the ability of the reduced-order models to predict non-planar crack growth corresponding to the load history not included in Table 4, a new load history has been tested with the load types: [4 2 3 5 1 3 3 5] and the corresponding number of cycles: [31779 15368 21222 16991 35515 32736 50430 17933]. The first two load types of

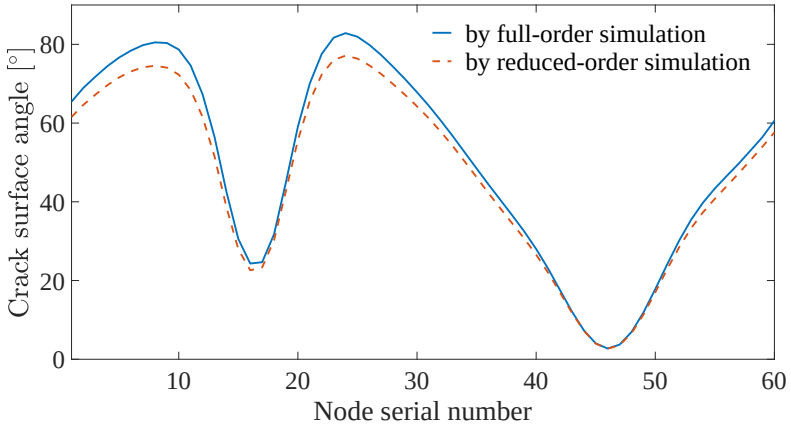

Fig. 15 Comparison of the crack surface angle by the proposed reduced-order model and full-order SGBEM-FEM coupling simulation for the first growth history.

Table 6 The test error of the reduced-order models for the five test growth histories

	Proposed surface-based		Front curve-based	
The number of growth history for test	e_k^d (mm)	e_k^θ $([^\circ])$	e_k^d (mm)	e_k^θ $([^\circ])$
1	**1.016e-3**	**3.474**	1.394e-3	10.149
2	**4.669e-4**	**3.046**	1.304e-3	6.418
3	**2.931e-3**	**9.132**	5.109e-3	12.689
4	**1.597e-3**	**3.492**	4.028e-3	6.930
5	**5.451e-4**	**6.156**	1.787e-3	8.709

this load history are the same as the first two load types of the 6th load history in Table 4, and the rest of the load types are different. A comparison of its full-order and reduced-order simulation results is shown in Fig. 16.

Observing the results, it becomes evident that the reduced-order models exhibit favorable agreement with the full-order model when predicting the initial crack growth. However, a noticeable discrepancy arises between the reduced-order model and the full-order simulation for the subsequent crack growth prediction. This disparity stems from the inherent variability in the 3D space of the crack surface, which presents challenges in accurately predicting the diverse forms of non-planar crack growth using the limited training samples available. This observation further underscores the substantial significance of load history on the reduced-order prognosis of three-dimensional non-planar crack growth, thereby emphasizing the necessity for in-depth exploration in subsequent investigations.

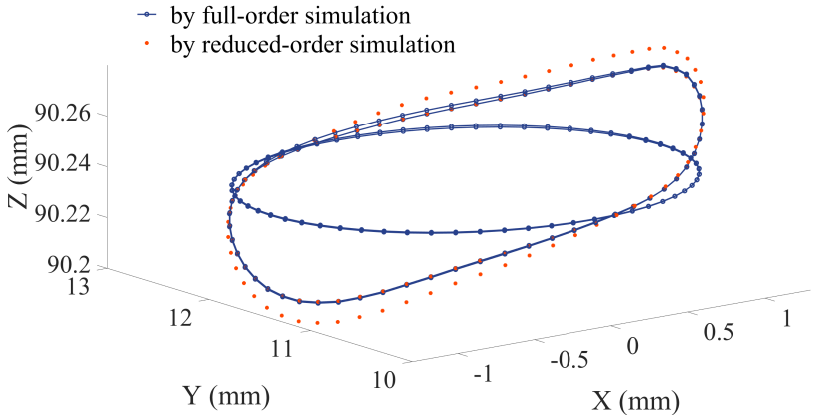

Fig. 16 Reduced-order models predictions for a load history outside the dataset.

B. Probabilistic Crack Growth Analysis Using Monte Carlo Simulation

The ROM developed in this paper can be seamlessly integrated into a probabilistic digital twin framework for analyzing non-planar crack growth. To illustrate this integration, we provide a demonstration of performing probabilistic non-planar crack growth analysis utilizing the ROM in conjunction with Monte Carlo methods.

In the realm of probabilistic analysis, it is imperative to account for various sources of uncertainty inherent in crack growth prediction. These uncertainties stem from factors such as errors in SIF prediction, load measurement inaccuracies, and material property variability.

To address SIF prediction uncertainty, the fitting error is taken into account by augmenting K_I and K_{II} at each node on the crack front with Gaussian noise: $K_I = K_I + N\left(0, \left(K_I \varepsilon_{K_I}\right)^2\right)$ and $K_{II} = K_{II} + N\left(0, \varepsilon_{K_{II}}^2\right)$. Furthermore, to incorporate the impact of load measurement errors, this study assumes that the errors follow a normal distribution characterized by a mean value of 0 and a standard deviation of $\sigma_L = 0.5N \cdot m$. Consequently, when calculating SIFs using Eqs. (9)-(10), the values of B and T are drawn from $N\left(B_{obs}, \sigma_L^2\right)$ and $N\left(T_{obs}, \sigma_L^2\right)$, where B_{obs} and T_{obs}

represent the observed values of B and T, respectively.

The uncertainty inherent in the fatigue model parameters is also taken into consideration. With reference to the linear relationship between the exponent and the coefficient in the power law equation of fatigue crack growth [48], the joint prior distribution of C and m is defined as:

$$\left[\begin{array}{c} \log C \\ m \end{array}\right]\Bigg|_{t=0} \sim N\left(\left[\begin{array}{c} -12.1844 \\ 3.8863 \end{array}\right], \left[\begin{array}{cc} 0.5 & -0.3 \\ -0.3 & 0.5 \end{array}\right]\right)$$

Here, $\log C$ is used instead because C is a very small value compared to other quantities.

In the Monte Carlo simulation, 2000 samples are randomly drawn from the prior distribution. Taking the seventh load history in Table 4 as an example (in order to simulate the realistic online deploy, the number of cycles corresponding to each load type is set to a definite value), 2000 crack growth histories are calculated.

To characterize the distribution of non-planar cracks, the characteristic size of non-planar cracks is defined as the distance between the farthest pairs of nodes along the crack front, e.g., between nodes (1 31), (2 32), ..., (30 60) (as shown in Fig. 17), are calculated according to [49, 50], and the maximum value is taken as the size of the current non-planar crack.

Fig. 18 shows the probability density function (PDF) of the final 2000 crack sizes. It can be seen that the crack size has a certain uncertainty, indicating the influence of uncertain factors on crack growth. At the same time, the PDF has a long tail region because the crack growth rates are faster for the samples assigned with larger fatigue model parameters. The uncertainty of this crack size distribution needs to be controlled in future studies by diagnosis in the digital twin framework. Furthermore, it is noteworthy that while a full-order simulation for this Monte Carlo simulation would take approximately 53 days, the ROM-based prediction presented here requires only about 5 hours, thus highlighting a substantial improvement in computational efficiency.

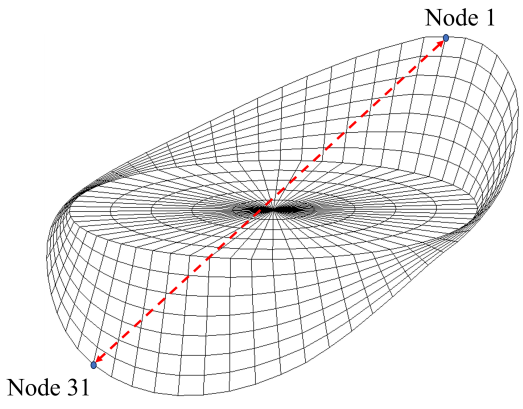

Fig. 17 The distance between a set of farthest nodes on the crack front.

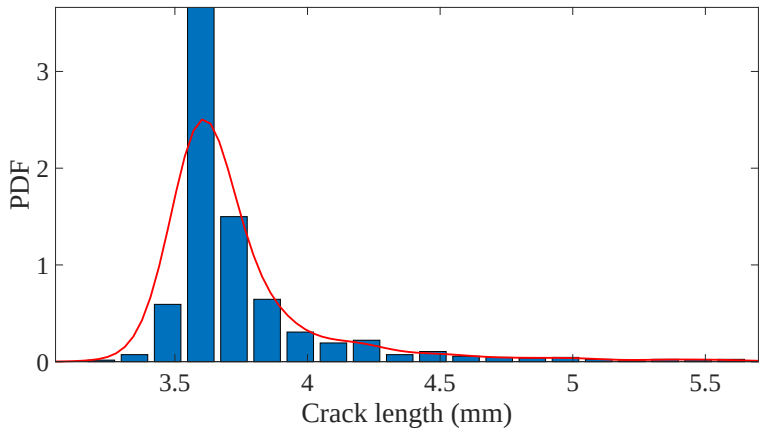

Fig. 18 Probability density function of the crack size considering uncertainties.

V. Conclusions

This paper introduces a novel reduced-order modeling method that considers the entire morphology of crack surfaces to achieve rapid prediction of non-planar crack growth. This approach capitalizes on the synergies between the SGBEM super element-FEM assembly coupling method for fracture mechanics simulations and the precise representation of complete crack surfaces using B-spline surfaces.

The process for constructing the reduced-order model for predicting SIFs of 3D non-planar cracks in the offline stage is described. This process relies on a B-spline surface representation and employs a combination of K-means clustering, principal component analysis, and Gaussian process regression. The online deployment of the ROM for deterministic and probabilistic crack growth analysis is also showcased. A cylindrical component resembling a rotorcraft mast is employed as a case study. The proposed method was demonstrated to have high accuracy through comparisons of crack growth histories obtained from the reduced-order model with those obtained from the full-order simulation. The efficiency of the reduced-order simulation was shown to be three orders of magnitude greater than that of the full-order simulation, providing a foundation for future digital twin research.

In future studies, the proposed three-dimensional reduced-order model for non-planar crack growth will be integrated with advanced damage detection techniques to form a digital twin for the diagnosis and prognosis of complex non-planar cracks. Furthermore, the investigation of crack growth in composite structures with complex geometries will also be a topic of interest in our future research efforts.

Appendix

In this study, the number of clusters is set to 12, as shown in Section III. Here, the impact of varying cluster numbers is considered. Fig. 19 displays the outcomes of clustering using the K-means algorithm for 10, 11, 12, 13, and 14 clusters. Notably, it is observed that, starting from 12 clusters, the samples positioned in the upper-right corner are

divided into two clusters.

Table 7 provides insights into the number of crack samples and the associated fitting errors of stress intensity factors in the upper-right cluster across different cluster quantities. A significant reduction in the count of crack samples within the upper-right cluster is noted when transitioning from 12 clusters. This reduction indicates a more rational distribution of crack samples with distinct spatial characteristics into diverse clusters, leading to a corresponding diminution in fitting errors for stress intensity factors.

Additionally, the upper-right cluster corresponds to the location where crack growth begins, and the precision of training for this cluster significantly influences the prediction accuracy of subsequent crack growth stages. Consequently, the number of clusters is set to 12.

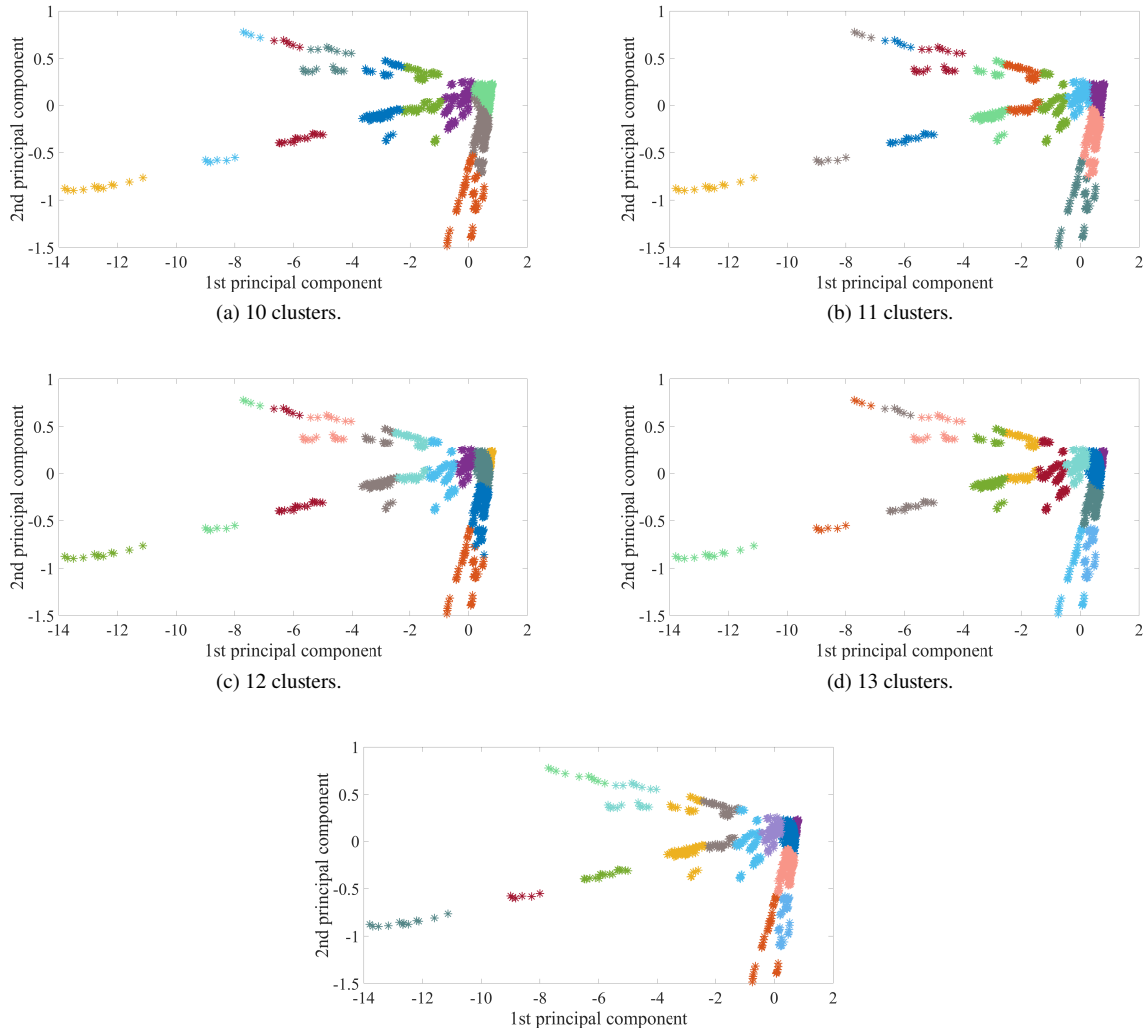

(a) 10 clusters.

(b) 11 clusters.

(c) 12 clusters.

(d) 13 clusters.

(e) 14 clusters.

Fig. 19 Different cluster numbers generated by the K-means algorithm.

Table 7 The number of crack samples and the fitting errors of stress intensity factors in the upper-right cluster for different number of clusters

Number of clusters	Number of crack samples	$\varepsilon_{K_I}(\%)$	$\varepsilon_{K_{II}}(MPa\sqrt{m})$
10	950	6.67	0.3114
11	941	6.67	0.3108
12	375	3.73	0.2553
13	371	3.73	0.2546
14	363	3.71	0.2527

Acknowledgement

The National Natural Science Foundation of China (grant number 12072011), the Aeronautical Science Foundation of China (grant number 201909051001) supported the work of the authors. The China Scholarship Council (grant number 202106020002) and the Academic Excellence Foundation of Beihang University for Ph.D. Students supported the work of the second author.

References

[1] Lee, H., Cho, H., and Park, S., "Review of the F-16 Individual Aircraft Tracking Program," *Journal of Aircraft*, Vol. 49, No. 5, 2012, pp. 1398–1405. https://doi.org/10.2514/1.C031692.

[2] Zhao, F., Zhou, X., Wang, C., Dong, L., and Atluri, S. N., "Setting Adaptive Inspection Intervals in Helicopter Components, Based on a Digital Twin," *AIAA Journal*, Vol. 61, No. 6, 2023, pp. 2675–2688. https://doi.org/10.2514/1.J062222.

[3] Glaessgen, E., and Stargel, D., "The Digital Twin Paradigm for Future NASA and U.S. Air Force Vehicles," *53rd AIAA/ASME/ASCE/AHS/ASC Structures, Structural Dynamics and Materials Conference 20th AIAA/ASME/AHS Adaptive Structures Conference 14th AIAA*, 2012, p. 1818. https://doi.org/10.2514/6.2012-1818.

[4] Cheung, C., and Bellinger, N. C., "Roadmap for Helicopter Life Usage Monitoring," *Thirteenth Australian International Aerospace Congress*, Royal Aeronautical Soc., Melbourne, Australia, 2009, pp. 1–13.

[5] Zhou, X., He, S., Dong, L., and Atluri, S. N., "Real-Time Prediction of Probabilistic Crack Growth with a Helicopter Component Digital Twin," *AIAA Journal*, Vol. 60, No. 4, 2022, pp. 2555–2567. https://doi.org/10.2514/1.J060890.

[6] Zhou, X., Sbarufatti, C., Giglio, M., Dong, L., and Atluri, S. N., "Copula-Based Collaborative Multistructure Damage Diagnosis and Prognosis for Fleet Maintenance Digital Twins," *AIAA Journal*, Vol. 0, No. 0, 0, pp. 1–6. https://doi.org/10.2514/1.J063105.

[7] Li, C., Mahadevan, S., Ling, Y., Choze, S., and Wang, L., "Dynamic Bayesian Network for Aircraft Wing Health Monitoring Digital Twin," *AIAA Journal*, Vol. 55, No. 3, 2017, pp. 930–941. https://doi.org/10.2514/1.J055201.

[8] Kapteyn, M. G., Pretorius, J. V., and Willcox, K. E., "A Probabilistic Graphical Model Foundation for Enabling Predictive

Digital Twins at Scale," *Nature Computational Science*, Vol. 1, No. 5, 2021, pp. 337–347. https://doi.org/10.1038/s43588-021-00069-0.

[9] Li, T., Lomazzi, L., Cadini, F., Sbarufatti, C., Chen, J., and Yuan, S., "Numerical Simulation-Aided Particle Filter-Based Damage Prognosis Using Lamb Waves," *Mechanical Systems and Signal Processing*, Vol. 178, 2022, p. 109326. https://doi.org/10.1016/j.ymssp.2022.109326.

[10] Li, T., Sbarufatti, C., Cadini, F., Chen, J., and Yuan, S., "Particle Filter-Based Hybrid Damage Prognosis Considering Measurement Bias," *Structural Control and Health Monitoring*, Vol. 29, No. 4, 2022, p. e2914. https://doi.org/10.1002/stc.2914.

[11] Hombal, V., and Mahadevan, S., "Surrogate Modeling of 3D Crack Growth," *International Journal of Fatigue*, Vol. 47, 2013, pp. 90–99. https://doi.org/10.1016/j.ijfatigue.2012.07.012.

[12] Yaren, M. F., Demir, O., Ayhan, A. O., and İriç, S., "Three-Dimensional Mode-I/III Fatigue Crack Propagation: Computational Modeling and Experiments," *International Journal of Fatigue*, Vol. 121, 2019, pp. 124–134. https://doi.org/10.1016/j.ijfatigue.2018.12.005.

[13] Moës, N., Gravouil, A., and Belytschko, T., "Non-Planar 3D Crack Growth by the Extended Finite Element and Level Sets—Part I: Mechanical Model," *International Journal for Numerical Methods in Engineering*, Vol. 53, No. 11, 2002, pp. 2549–2568. https://doi.org/10.1002/nme.429.

[14] Gravouil, A., Moës, N., and Belytschko, T., "Non-Planar 3D Crack Growth by the Extended Finite Element and Level Sets—Part II: Level Set Update," *International Journal for Numerical Methods in Engineering*, Vol. 53, No. 11, 2002, pp. 2569–2586. https://doi.org/10.1002/nme.430.

[15] Shi, J., Chopp, D., Lua, J., Sukumar, N., and Belytschko, T., "Abaqus Implementation of Extended Finite Element Method Using a Level Set Representation for Three-Dimensional Fatigue Crack Growth and Life Predictions," *Engineering Fracture Mechanics*, Vol. 77, No. 14, 2010, pp. 2840–2863. https://doi.org/10.1016/j.engfracmech.2010.06.009.

[16] Passieux, J.-C., Réthoré, J., Gravouil, A., and Baietto, M.-C., "Local/Global Non-Intrusive Crack Propagation Simulation Using a Multigrid X-FEM Solver," *Computational Mechanics*, Vol. 52, No. 6, 2013, pp. 1381–1393. https://doi.org/10.1007/s00466-013-0882-3.

[17] Bordas, S., Rabczuk, T., and Zi, G., "Three-Dimensional Crack Initiation, Propagation, Branching and Junction in Non-Linear Materials by an Extended Meshfree Method without Asymptotic Enrichment," *Engineering Fracture Mechanics*, Vol. 75, No. 5, 2008, pp. 943–960. https://doi.org/10.1016/j.engfracmech.2007.05.010.

[18] Rabczuk, T., and Belytschko, T., "Cracking Particles: a Simplified Meshfree Method for Arbitrary Evolving Cracks," *International Journal for Numerical Methods in Engineering*, Vol. 61, No. 13, 2004, pp. 2316–2343. https://doi.org/10.1002/nme.1151.

[19] Bichon, B. J., Eldred, M. S., Swiler, L. P., Mahadevan, S., and McFarland, J. M., "Efficient Global Reliability Analysis for Nonlinear Implicit Performance Functions," *AIAA Journal*, Vol. 46, No. 10, 2008, pp. 2459–2468. https://doi.org/10.2514/1.34321.

[20] Jones, D. R., Schonlau, M., and Welch, W. J., "Efficient Global Optimization of Expensive Black-Box Functions," *Journal of Global Optimization*, Vol. 13, No. 4, 1998, pp. 455–492. https://doi.org/10.1023/A:1008306431147.

[21] Sacks, J., Welch, W. J., Mitchell, T. J., and Wynn, H. P., "Design and Analysis of Computer Experiments," *Statistical Science*, Vol. 4, No. 4, 1989, pp. 409–423. https://doi.org/10.1214/ss/1177012413.

[22] Simpson, T. W., Lin, D. K., and Chen, W., "Sampling Strategies for Computer Experiments: Design and Analysis," *International Journal of Reliability and Applications*, Vol. 2, No. 3, 2001, pp. 209–240. URL https://koreascience.kr/article/JAKO200111921705473.page.

[23] Simpson, T. W., Poplinski, J., Koch, P. N., and Allen, J. K., "Metamodels for Computer-Based Engineering Design: Survey and Recommendations," *Engineering with Computers*, Vol. 17, No. 2, 2001, pp. 129–150. https://doi.org/10.1007/PL00007198.

[24] Leser, P. E., Hochhalter, J. D., Warner, J. E., Newman, J. A., Leser, W. P., Wawrzynek, P. A., and Yuan, F.-G., "Probabilistic Fatigue Damage Prognosis Using Surrogate Models Trained via Three-Dimensional Finite Element Analysis," *Structural Health Monitoring*, Vol. 16, No. 3, 2017, pp. 291–308. https://doi.org/10.1177/1475921716643298.

[25] Leser, P. E., Warner, J. E., Leser, W. P., Bomarito, G. F., Newman, J. A., and Hochhalter, J. D., "A Digital Twin Feasibility Study (Part II): Non-Deterministic Predictions of Fatigue Life Using In-Situ Diagnostics and Prognostics," *Engineering Fracture Mechanics*, Vol. 229, 2020, p. 106903. https://doi.org/10.1016/j.engfracmech.2020.106903.

[26] Ananthasayanam, B., Loghin, A., and Subramaniyan, A. K., "An Efficient Framework for Rapid Life Assessment in Industrial Applications: Fatigue Crack Growth," *Engineering Fracture Mechanics*, Vol. 181, 2017, pp. 7–28. https://doi.org/10.1016/j.engfracmech.2017.06.016.

[27] Spear, A. D., Priest, A. R., Veilleux, M. G., Ingraffea, A. R., and Hochhalter, J. D., "Surrogate Modeling of High-Fidelity Fracture Simulations for Real-Time Residual Strength Predictions," *AIAA Journal*, Vol. 49, No. 12, 2011, pp. 2770–2782. https://doi.org/10.2514/1.J051159.

[28] Loop, C. T., and DeRose, T. D., "A Multisided Generalization of Bézier Surfaces," *ACM Transactions on Graphics (TOG)*, Vol. 8, No. 3, 1989, pp. 204–234. https://doi.org/10.1145/77055.77059.

[29] Warren, J., "Creating Multisided Rational Bézier Surfaces Using Base Points," *ACM Transactions on Graphics (TOG)*, Vol. 11, No. 2, 1992, pp. 127–139. https://doi.org/10.1145/130826.130828.

[30] Yang, L., and Zeng, X.-M., "Bézier Curves and Surfaces with Shape Parameters," *International Journal of Computer Mathematics*, Vol. 86, No. 7, 2009, pp. 1253–1263. https://doi.org/10.1080/00207160701821715.

[31] Gordon, W. J., and Riesenfeld, R. F., "B-spline Curves and Surfaces," *Computer Aided Geometric Design*, Academic Press, 1974, pp. 95–126. https://doi.org/10.1016/B978-0-12-079050-0.50011-4.

[32] Catmull, E., and Clark, J., "Recursively Generated B-Spline Surfaces on Arbitrary Topological Meshes," *Computer-Aided Design*, Vol. 10, No. 6, 1978, pp. 350–355. https://doi.org/10.1016/0010-4485(78)90110-0.

[33] Milroy, M. J., Bradley, C., Vickers, G. W., and Weir, D., "G1 Continuity of B-Spline Surface Patches in Reverse Engineering," *Computer-Aided Design*, Vol. 27, No. 6, 1995, pp. 471–478. https://doi.org/10.1016/0010-4485(95)00020-R.

[34] Piegl, L., and Tiller, W., *The NURBS Book*, Springer-Verlag, New York, NY, USA, 1996. https://doi.org/10.1007/978-3-642-97385-7.

[35] Ma, W., and Kruth, J.-P., "NURBS Curve and Surface Fitting for Reverse Engineering," *The International Journal of Advanced Manufacturing Technology*, Vol. 14, No. 12, 1998, pp. 918–927. https://doi.org/10.1007/BF01179082.

[36] Dan, J., and Lancheng, W., "An Algorithm of NURBS Surface Fitting for Reverse Engineering," *The International Journal of Advanced Manufacturing Technology*, Vol. 31, No. 1, 2006, pp. 92–97. https://doi.org/10.1007/s00170-005-0161-3.

[37] Hectors, K., and Waele, W. D., "An X-FEM Based Framework for 3D Fatigue Crack Growth Using a B-Spline Crack Geometry Description," *Engineering Fracture Mechanics*, Vol. 261, 2022, p. 108238. https://doi.org/10.1016/j.engfracmech.2022.108238.

[38] Bingol, O. R., and Krishnamurthy, A., "NURBS-Python: An Open-Source Object-Oriented NURBS Modeling Framework in Python," *SoftwareX*, Vol. 9, 2019, pp. 85–94. https://doi.org/10.1016/j.softx.2018.12.005.

[39] Dong, L., and Atluri, S. N., "SGBEM(Using Non-Hyper-Singular Traction BIE), and Super Elements, for Non-Collinear Fatigue-Growth Analyses of Cracks in Stiffened Panels with Composite-Patch Repairs," *Computer Modeling in Engineering & Sciences(CMES)*, Vol. 89, No. 5, 2012, pp. 415–456. https://doi.org/10.3970/cmes.2012.089.417.

[40] Dong, L., and Atluri, S. N., "Fracture & Fatigue Analyses: SGBEM-FEM or XFEM? Part 1: 2D Structures," *CMES-Computer Modeling in Engineering and Sciences*, Vol. 90, No. 2, 2013, pp. 91–146. https://doi.org/10.3970/cmes.2013.090.091.

[41] Dong, L., and Atluri, S. N., "Fracture & Fatigue Analyses: SGBEM-FEM or XFEM? Part 2: 3D Solids," *CMES-Computer Modeling in Engineering and Sciences*, Vol. 90, No. 5, 2013, pp. 379–413. https://doi.org/10.3970/cmes.2013.090.379.

[42] Erdogan, F., and Sih, G. C., "On the Crack Extension in Plates Under Plane Loading and Transverse Shear," *Journal of Basic Engineering*, Vol. 85, No. 4, 1963, pp. 519–525. https://doi.org/10.1115/1.3656897.

[43] Tanaka, K., "Fatigue Crack Propagation from a Crack Inclined to the Cyclic Tensile Axis," *Engineering Fracture Mechanics*, Vol. 6, No. 3, 1974, pp. 493–507. https://doi.org/10.1016/0013-7944(74)90007-1.

[44] Hartigan, J. A., and Wong, M. A., "Algorithm AS136: A K-Means Clustering Algorithm," *Applied Statistics*, Vol. 28, No. 1, 1979, pp. 100–108. https://doi.org/10.2307/2346830.

[45] Ko, J., and Fox, D., "GP-BayesFilters: Bayesian Filtering Using Gaussian Process Prediction and Observation Models," *Autonomous Robots*, Vol. 27, No. 1, 2009, pp. 75–90. https://doi.org/10.1109/IROS.2008.4651188.

[46] Rasmussen, C. E., "Gaussian Processes in Machine Learning," *Summer School on Machine Learning*, Springer, Springer-Verlag, New York, NY, USA, 2003, pp. 63–71.

[47] Amato, D., Mayrhofer, L., Robl, C., Dhondt, G., and Citarella, R., "Prediction of the Crack Growth Propagation Direction in Non-Proportional Mixed-Mode Missions," *International Journal of Fatigue*, Vol. 166, 2023, p. 107233. https://doi.org/10.1016/j.ijfatigue.2022.107233.

[48] Bergner, F., and Zouhar, G., "A new approach to the correlation between the coefficient and the exponent in the power law equation of fatigue crack growth," *International Journal of Fatigue*, Vol. 22, No. 3, 2000, pp. 229–239. https://doi.org/10.1016/S0142-1123(99)00123-1.

[49] Hombal, V., Wolfe, K., Ling, Y., and Mahadevan, S., "Uncertainty Quantification In Non-planar Crack Growth Analysis," *53rd AIAA/ASME/ASCE/AHS/ASC Structures, Structural Dynamics and Materials Conference 20th AIAA/ASME/AHS Adaptive Structures Conference 14th AIAA*, 2012, p. 1541. https://doi.org/10.2514/6.2012-1541.

[50] Hombal, V., Ling, Y., Wolfe, K., and Mahadevan, S., "Two-stage planar approximation of non-planar crack growth," *Engineering Fracture Mechanics*, Vol. 96, 2012, pp. 147–164. https://doi.org/10.1016/j.engfracmech.2012.07.017.